

1 Towards predictive nanotoxicology: from roundabout of molecular 2 events to chronic inflammation prediction

3 Authors:

4 Hana Majaron*, Boštjan Kokot*, Aleksandar Sebastijanović*, Carola Voss, Rok Podlipec, Patrycja Zawilska,
5 Trine Berthing, Carolina Ballester, Pernille Høgh Danielsen, Claudia Contini, Mikhail Ivanov, Ana Krišelj,
6 Petra Čotar, Qiaoxia Zhou, Jessica Ponti, Vadim Zhernovkov, Matthew Schneemilch, Mojca Pušnik, Polona
7 Umek, Stane Pajk, Olivier Joubert, Otmar Schmid, Iztok Urbančič, Martin Irmler, Johannes Beckers, Vladimir
8 Lobaskin, Sabina Halappanavar, Nicholas Quirke, Alexander Lyubartsev, Ulla Vogel, Tilen Koklič**, Tobias
9 Stöger**, Janez Štrancar**

10

11 Abstract

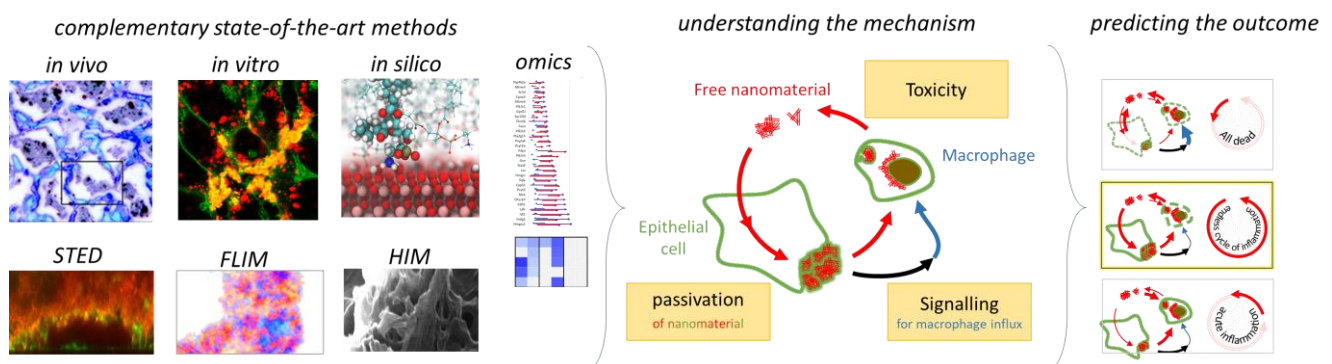
12

13 Many chronic diseases manifest themselves in prolonged inflammation and often ignored dysregulated lipid
14 metabolism, both also associated with inhalation of certain nanomaterials. Limited knowledge of involved
15 molecular events and their causal connections prevents reliable prediction of outcomes by efficient testing
16 strategies. To unravel how acute nanomaterial exposure leads to chronic conditions, we employed advanced
17 microscopy and omics *in vitro*, *in vivo* and *in silico*. For selected metal-oxide nanomaterials, we show that
18 epithelial cells survive the exposure by excreting internalized nanomaterials and passivating them on the surface,
19 employing elevated lipid synthesis. Macrophages, on the contrary, attack the defending epithelium but die
20 degrading passivized complexes, releasing nanomaterial, which is reuptaken by epithelial cells. Constant
21 proinflammatory signalling recruits new phagocytes that feed the vicious cycle of events resulting in a long-
22 lasting response to a single exposure. The discovered mechanism predicts the nanomaterial-associated *in vivo*
23 chronic outcomes based on simple *in vitro* measurements and potentially enlightens other chronic diseases.

24

25 Graphical abstract

26



27

28

29 Introduction - Mechanism of persistent inflammation unknown

30

31 Today, chronic diseases such as asthma, lung cancer, heart disease, and brain damage with accelerated cognitive
32 decline, are considered to be some of the most significant causes of death¹⁻³. Despite the lack of understanding
33 how these adverse outcomes evolve, they are known to be associated with air pollution and inhalation of
34 particulate matter and nanoparticles⁴. According to the OECD and WHO, inhaled particulate matter kills four

35 million people globally every year ^{5,6}. In addition, the ever-increasing production of nanomaterials, as
36 consequence of the rapidly developing and extremely promising nanotechnology industry, generates concerns
37 about potential human exposure and health impacts. Decision-makers around the world (OECD, US EPA, NIH,
38 EC, JRC, etc.) recognized the need for elucidating molecular mechanisms involved in possible adverse outcome
39 pathways (AOPs) ⁷. The later has emerged as the most promising conceptual construct towards predictive
40 toxicology elucidating the key events of respective toxicity pathways to improve the prediction of the apical
41 endpoints with alternative testing strategies ⁸.

42 Despite some important advances using multiple cell-line *in vitro* test systems ⁹ in the field of nanotoxicology,
43 the desired mechanism-based *in vitro* assays and *in silico* predictive tools have not yet reached the required level
44 of maturity and reliability ¹⁰. This is especially true for alternative testing strategies addressing chronic outcomes
45 ¹¹, that are inherently associated with a long-term development of pathophysiological changes. In this case, the
46 complicity of long-term in-vitro exposures, together with the lack of understanding of the underlying
47 mechanisms and the associated molecular events behind the AOPs, completely precludes the prediction of
48 chronic outcomes.

49 Upon pulmonary exposure, some nanomaterials have been shown to induce exceptionally long lasting chronic
50 inflammatory responses, which is reflected in prolonged accumulation of infiltrated leukocytes in the lungs
51 following a single nanomaterial exposure event ¹²⁻¹⁷ or chronic inhalation of relatively low nanomaterial
52 concentrations ¹⁸⁻²⁰. The insolubility and biopersistence of the particles combined with continuous release of
53 pro-inflammatory mediators from irritated resident cells or dying immune cells could explain a perpetuation of
54 inflammation in the above-mentioned chronic response, which is frequently co-observed with chronic
55 dysregulated lipid metabolism ²¹⁻²⁶.

56 Here we show that a minimal combination of *in vitro* and *in silico* tests can explain and reproduce chronically
57 dysregulated lipid metabolism accompanying chronic inflammation, which originates in nanomaterial cycling
58 between passivated form on epithelial cells and bare form released from dying immune cells.

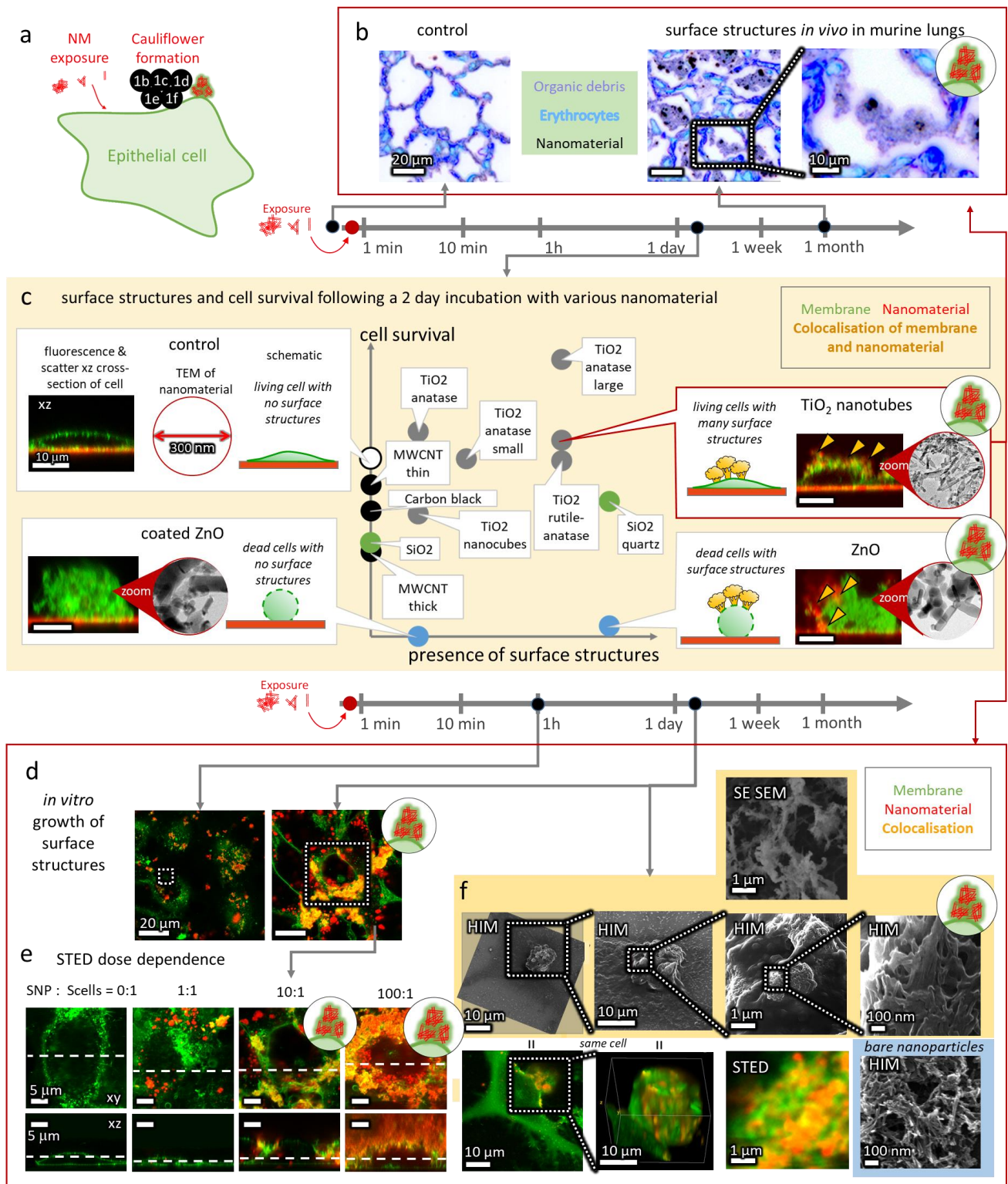
59

60 Results and discussion

61

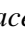
62 1. Passivation of nanomaterials

63



64

65 **Fig. 1: Formation of cauliflowers (bio-nano agglomerates) on epithelial cell surface.** *a* A general scheme of
 66 events shown in this figure. *b* Cytoviva dark-field scattering micrographs of bio-nano agglomerates observed
 67 on alveolar walls after instillation of mice with TiO₂ nanotubes (black and violet intermixed). In fluorescence
 68 micrographs *c-f* membranes are green and nanoparticles red. *c* Presence of surface structures, cell survival
 69 and cross-sections of alveolar epithelial (LA-4) cells after a 2-day exposure to several nanomaterials at
 70 nanomaterial-to-cell surface ratio of 10:1 (nanoparticles observed in backscatter). Inserts show 300 nm-large
 71 TEM micrographs of nanoparticles used. *d* Time-dependent cauliflower formation by LA-4 exposed to TiO₂
 72 nanotubes at surface ratio of 10:1. *e* Super-resolved STED *xy* and *xz* cross-sections of dose-dependent
 73 cauliflower growth reveal that cauliflowers are located on the outer surface of cells after 2 days. The surface-

74 to-surface ratios are 0:1, 1:1, 10:1 and 100:1. **f**  High-resolution correlative STED, SE SEM and HIM images
 75 reveal the detailed structures of cauliflowers (arrowheads) at a surface dose of 10:1. For associated data see
 76 Supp. info S1.

77

78 To uncover the causal relationships of events leading from pulmonary nanomaterial exposure to chronic
 79 inflammation, we applied a complex set of *in vivo*, *in vitro* and *in silico* experiments employing state-of-the-art
 80 microscopy, spectroscopy, omics and modelling approaches. TiO₂ nanotubes were selected as the model
 81 nanomaterial, as they induce very high and long-lasting chronic inflammatory responses *in vivo* accompanied
 82 by markedly disturbed alveolar integrity of the lungs¹² with visible large bio-nano agglomerates on the alveolar
 83 walls (Fig. 1b, purple structures). Importantly, this nanomaterial induces similar large bio-nano agglomerate
 84 structures on the surface of the epithelial cells *in vitro* which remain viable for longer period (Fig. 1c), crucial
 85 for elucidating the mechanism *in vitro*. Note, that similar structures were observed both *in vivo* and *in vitro* after
 86 exposure to crystalline quartz (DQ12)¹², but not carbon nanotubes (CNTs)²⁶.

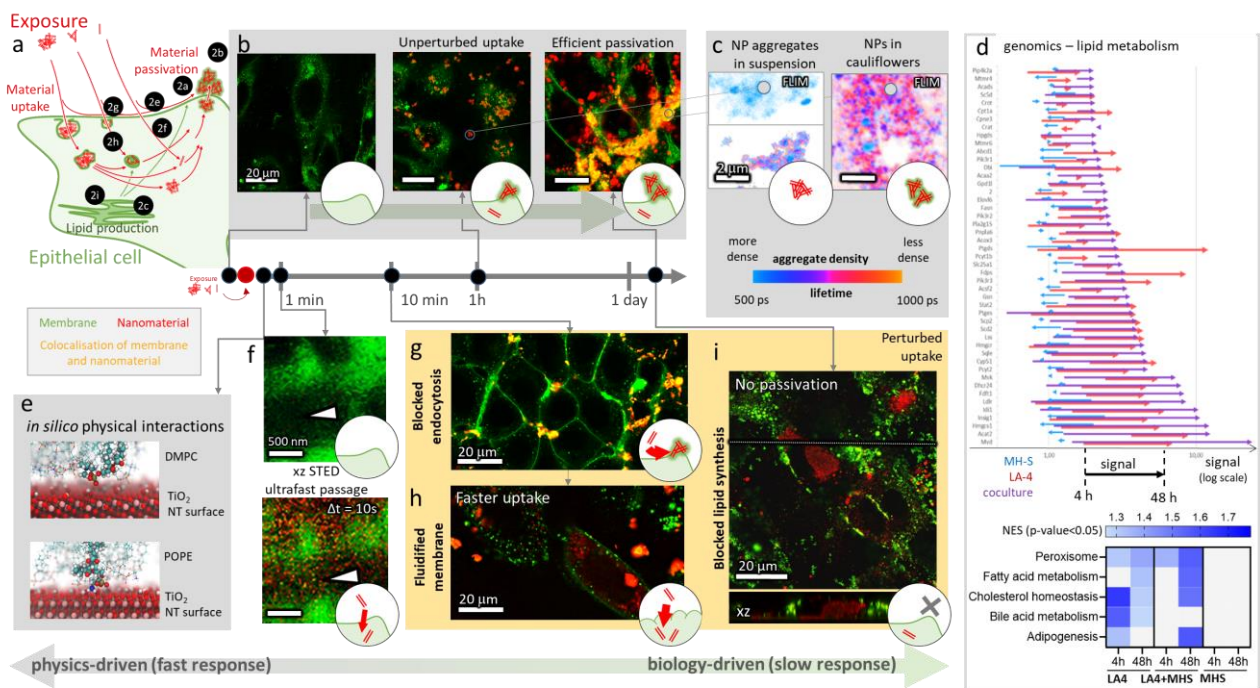
87 We have previously observed that TiO₂ nanotubes can wrap in parts of epithelial plasma membranes and relocate
 88 them efficiently across the epithelial layer²⁷ already at lower concentration of nanotubes (surface-of-
 89 nanomaterial-to-cell-surface dose 1:1) due to their high affinity for lipids. Thus, it is expected that at higher
 90 surface doses, these nanoparticles should completely disrupt the epithelial cell membranes. Surprisingly, our
 91 current experiments show that the epithelial cells survive exposures to surface doses as high as 100:1 (Fig. 1e,
 92 supplement section S0c and S0g). A few days after exposure, the majority of the nanoparticles are found in huge
 93 bio-nano agglomerates on the epithelial cell surface, consisting of at least nanoparticles and lipids, which we
 94 term cauliflowers due to their shape and yellow colour in our fluorescence micrographs (Fig. 1d, Fig. 1e, yellow
 95 colour).

96 Because cauliflowers are observed exclusively on the surface of epithelial cells, not inside (Fig. 1e, Fig. 1f),
 97 they might be driven solely by physical interactions between nanoparticles and lipids as in the case of lipid
 98 wrapping. However, the cauliflowers need one to two days to form, which suggests some involvement of active
 99 biological response.




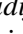

100

101

2. The role of lipids



102


103 **Fig. 2: Role of lipids in cauliflower formation.** *a* A general scheme of events shown in this figure. In
104 fluorescence micrographs, cell membranes are green and TiO₂ nanotubes red, surface dose was 10:1 (except
105 *f*). *b* Unperturbed uptake of TiO₂ nanotubes after 0, 1 h and 2 days by lung epithelial LA-4 cells, same as Fig.
106 1d. *c* Increased fluorescence lifetime (FLIM) of Alexa Fluor 647 on TiO₂ nanotubes in cauliflowers (right)
107 compared to agglomerates in suspension (left) corresponds to increased distance between fluorophores on the
108 nanotubes (e.g. separation due to lipid interspacing). *d* Transcriptomics analysis of lipid metabolism on the
109 gene level (top) and pathway level (bottom) for MH-S macrophages (blue), LA-4 epithelial cells (red) and their
110 co-culture (purple) after 4 hours (beginning of arrow) and 48 hours (end of arrow) of nanomaterial exposure.
111 *e* Final state of full-atom *in silico* simulation confirms strong interaction between disordered lipids and the TiO₂
112 nanotubes. *f*  Cross-sections immediately before (above) and 10 s after (below) instant delivery of TiO₂
113 nanotubes onto cells by nebulisation (1:1 surface dose) show ultrafast membrane passage of the nanotubes
114 through the cell plasma membrane into the cell (arrowhead), driven by pure physical interactions.
115 Pharmaceutical-perturbed uptakes (to compare with *b*): *g*   chlorpromazine-blocked clathrin-mediated
116 endocytosis, *h*  fluidified cell plasma membrane induced by cholesterol depletion (beta-methyl-cyclodextrin)
117 *i*  inhibited fatty acid synthesis (resveratrol-blocked fatty-acid synthase). For associated data see Supp. info
118 S2.

119

120 Coinciding with the formation of the lipid-rich bio-nano agglomerates (Fig. 2b), i.e. two days after the
121 nanomaterial exposure, a strong upregulation of membrane lipid metabolism-related genes is observed (Fig.
122 2d). Further modulation of the lipid synthesis pathway by blocking fatty acid synthase (FAS) with resveratrol
123 precludes the formation of large cauliflowers (Fig. 2i), confirming that epithelial cells usually respond to
124 nanomaterial exposure by an increased lipid synthesis, which is in turn required for cauliflower formation.

125 Because internalization of nanoparticles usually precedes cauliflower formation, we investigate the causality
126 between the two phenomena by blocking an important route of nanoparticle uptake, i.e. clathrin-mediated
127 endocytosis (supplement S0e), using chlorpromazine. Interestingly, small “proto” cauliflowers are formed soon
128 after exposure (15 min time scale) (Fig. 2g), indicating an additional mechanism of formation that requires no
129 intracellular processing. In this case, formation of cauliflowers presumably relies on the strong physical affinity
130 between nanoparticles and lipids, also supported by *in silico* simulations (Fig. 2e) and *in vitro* experiments on
131 model lipid membranes (S0d). However, these “proto” cauliflowers are rarely seen under normal conditions,
132 which lead us to conclude that this additional mechanism of formation is usually less probable, likely due to the
133 efficient particle uptake that displaces nanomaterial away from the plasma membrane, preventing their further
134 interaction.

135 Under unperturbed exposure (Fig. 2b), the basic physical interaction might therefore initiate the formation of
136 cauliflowers by driving nanoparticles and membrane lipids into small agglomerates anchored to the membrane.
137 The depletion of the functional lipid bilayer may trigger additional lipid synthesis, which later enables
138 passivation of even higher doses of nanoparticles in large agglomerates on the cellular surface (Fig. 1e).
139 Noteworthy, nanoparticles in these cauliflowers are effectively dissolved by interspaced lipids making them
140 more loosely packed compared to agglomerates of pure nanoparticles, as seen by increased fluorescence lifetime
141 (Fig. 2c).

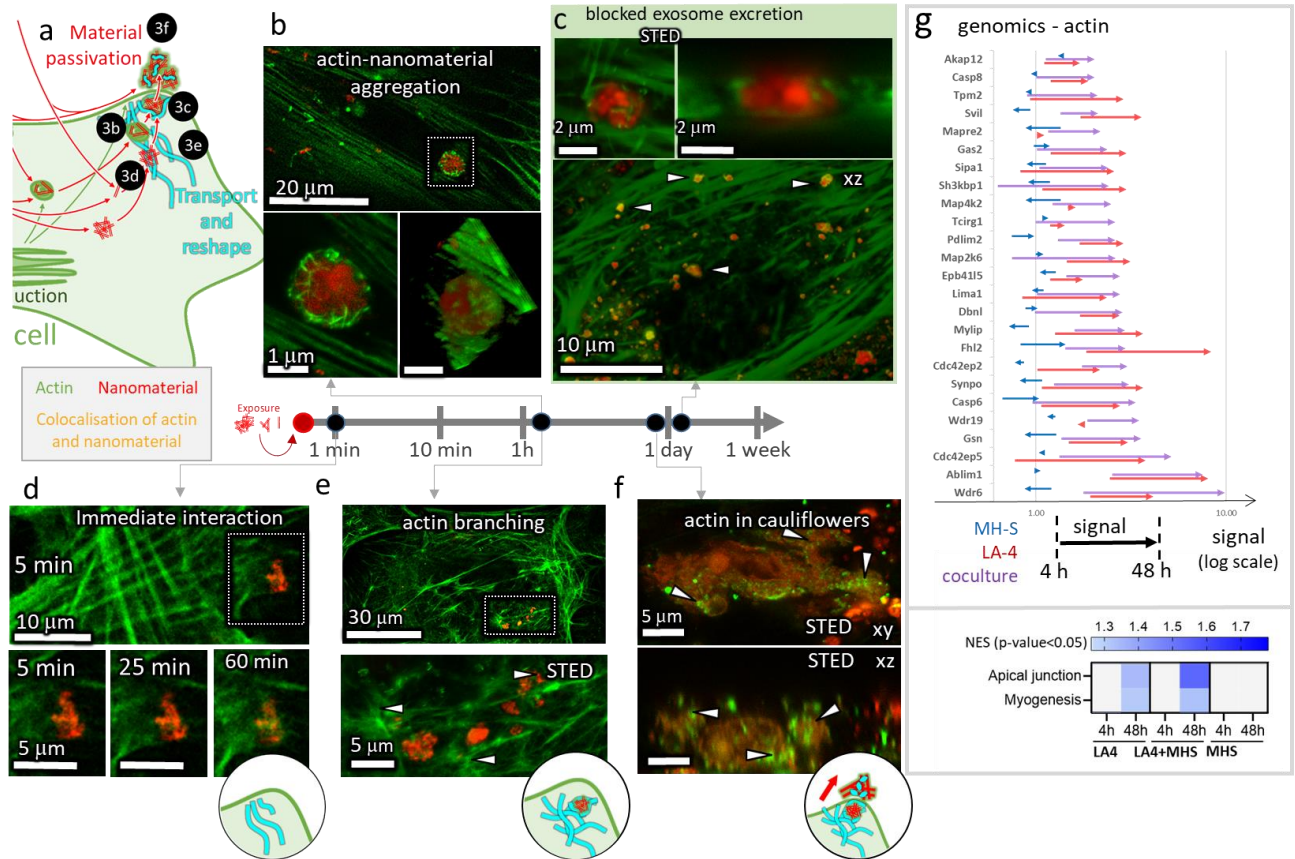
142 Interestingly, cholesterol depletion from the plasma membrane by beta-methyl-cyclodextrin (a cell membrane
143 fluidifying agent which also inhibits endocytosis) leads to strong suppression of fast (membrane-lipid-drain
144 only) cauliflower formation (Fig. 2h). This indicates an important interaction between nanoparticles and
145 cholesterol which is reflected also in strongly upregulated cholesterol synthesis pathways (Fig. 2d heatmap,
146 supplement S0), which is also seen *in vivo*¹². In the case of cholesterol-depleted plasma membranes, the majority
147 of nanoparticles pass the plasma membranes on a minute timescale, resulting in a fine distribution of particles
148 inside the cell. Interestingly, domination of such a passage can be observed also when nanoparticles are
149 delivered in a highly dispersed form through aerosol directly to the epithelial cell membranes and pass through
150 them in a matter of seconds (Fig. 2f, movie in supplement S0 .

151 For the lungs, the lipid-synthesis-driven formation of bio-nano agglomerates thus seems to be an active response
152 of alveolar epithelial cells, enabling their survival after exposure to nanomaterial even at higher doses. As such,

153 this process can be seen as passivation of nanomaterial, a kind of protection mechanism (S0f). The remaining
 154 question is the identification of the cellular mechanisms that can facilitate the export of the internalised material.

155

156 3. The role of actin




157

158 **Fig. 3: Role of actin in cauliflower formation.** a A general scheme of events shown in this figure. Fluorescence
 159 micrographs of the actin network of LA-4 cells (green) after exposure to TiO₂ nanotubes (red) at a 10:1 surface
 160 dose. d Soon after exposure, actin interacts with uptaken nanoparticles, b leading to formation of actin-
 161 nanoparticle agglomerates after a few hours. e Synchronously, the actin network branches (arrowheads),
 162 indicating changes in internal processes and reshaping of the cell. c Blocking the final stage of exocytosis with
 163 jasplakinolide traps nanoparticles in actin rings, prepared for exocytosis (arrowheads and zoom-ins). f After
 164 a few days, actin fragments are observed in cauliflowers (arrowheads). g Transcriptomics analysis of actin-
 165 network on the gene level (top) and pathway level (bottom) for LA-4 (red), macrophages (blue), and their co-
 166 cultures (purple) after 4 hours (beginning of arrow) and 48 hours (end of arrow) of nanomaterial exposure.
 167 For associated data see Supp. info S3.

168

169 Because exocytosis mechanisms involve cytoskeletal actin remodelling, the relevance of actin was investigated
 170 next. Almost simultaneously with nanoparticle uptake and far before cauliflowers can form, many nanoparticles
 171 evidently interact with actin fibres (Fig. 3d, movie in supplement S3d) , forming nanoparticle-actin 3D
 172 agglomerates resembling Faberge eggs (Fig. 3b, 3D in supplement S0b). Hours after exposure the same
 173 interaction causes actin network transformations from native to branched (Fig. 3e), indicating increased cell
 174 motility²⁸, internal vesicular trafficking^{29,30} and nanoparticles exocytosis^{31,32}.

175 By blocking actin fibre dynamics (polymerization and depolymerisation) with jasplakinolide, excretion of
 176 exocytotic vesicles can be stopped, enabling their visualisation and identification of their content. Namely, after
 177 uptake of nanoparticles and lipid synthesis, nanoparticles are trapped in exocytotic vesicles (actin rings),

178 prepared for exocytosis by the cell (Fig. 3c). Because lots of actin can be identified outside cells in cauliflowers
 179 (Fig. 3f ) , excretion of nanoparticles is seemingly more destructive to the actin network than normal
 180 exocytosis, where actin is retained inside cells. Actin adherence is also reflected in the coronome analysis of the
 181 mobile fraction of nanoparticles after exposure in which we have previously found abundant actin proteins ²⁷.
 182 This clearly coincides with upregulation of the actin synthesis pathway (Fig. 3g). Up to now, the appearance of
 183 actin in the nanoparticle corona outside of the cells could not be explained.

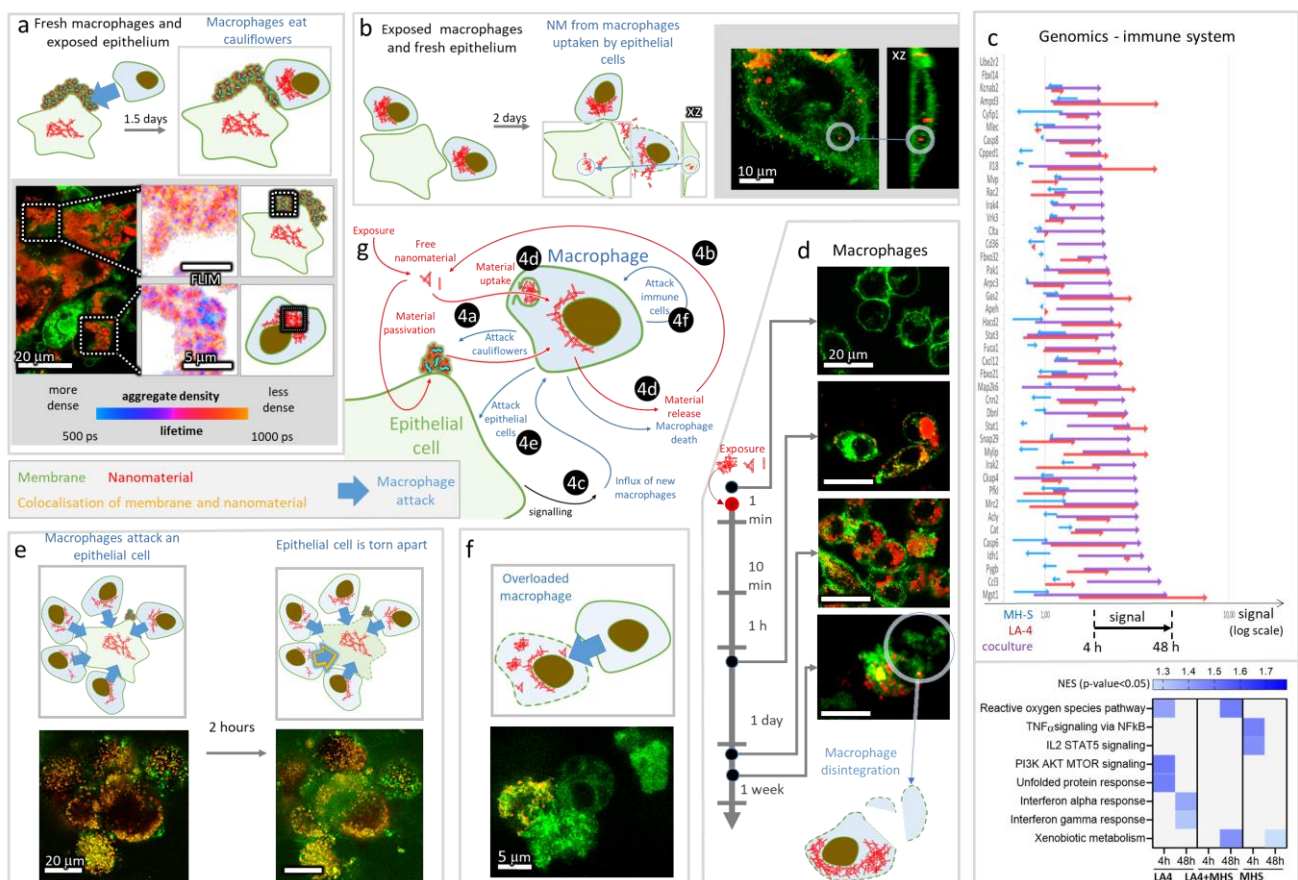
184 Creation of cauliflowers on the cell surface thus involves both membrane lipids and actin (Fig. 2d heatmap, Fig.
 185 3c) that clearly interact with the nanoparticle surface directly. Due to strong binding of amines and phosphates
 186 identified with *in silico* simulations (Fig. 2e) it is reasonable to expect that various biomolecules can strongly
 187 bind to the same surface, from lipids and proteins to nucleic acids. Moreover, multiple binding sites on
 188 nanomaterial and biomolecules directly lead to crosslinking and formation of large bio-nano agglomerates, such
 189 as the observed cauliflowers. This implies that any strong interaction identified within *in silico* modelling of
 190 biomolecule - nanomaterial surface pairs, is highly predictive of bio-nano agglomerates formation.

191 Ability to supply enough biomolecules to crosslink and thereby passivate the received dose of nanomaterial
 192 explains epithelial cell survival even at large local dose of nanomaterial seen *in vivo* (Fig.1). This, however,
 193 seems to be contradictory to the coinciding chronic inflammation, raising the question about the role of
 194 surrounding cells, especially macrophages, which are responsible for the immune defence within the alveoli. To
 195 address this, we expose a co-culture of LA-4 epithelial cells and MH-S macrophages in the same way as we did
 196 with the epithelial monoculture.

197


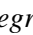
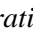
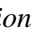
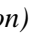

198 4. MH-S action against LA-4 defence


199






200

201 **Fig. 4: The cycle of uptake, passivation and release in nanomaterial-exposed co-culture. In all fluorescence**
 202 **micrographs, cell membranes are green and TiO₂ nanotubes red, and the surface dose of nanoparticles is 10:1.**

203 **a** Unexposed macrophages (MH-S) were added to washed LA-4 with cauliflowers. In 1.5 days, MH-S phagocyte
204 the cauliflowers from LA-4, and degrade the organic (lipid) part, compacting the nanoparticles (fluorescence-
205 lifetime-maps FLIM, right). **b** Washed nanomaterial-laden MH-S were added to unexposed LA-4. After 2 days,
206 nanomaterial is found in LA-4 (encircled). **c** Transcriptomics analysis of innate and adaptive immune system
207 on a gene level (top) and pathway level (bottom) for LA-4 (red), MH-S (blue) and their co-culture (purple) after
208 4 hours (beginning of arrow) and 48 hours (end of arrow) of nanomaterial exposure. **d** Nanoparticle uptake by
209 MH-S followed by their disintegration after a few days (encircled):  (control)  (2 h)  (2 days)  (4 days, MH-S disintegration) **e**  Time-lapse of MH-S attacking and tearing apart a nanomaterial-laden LA-
210 4 cell. **f**  MH-S observed attacking another nanomaterial-laden MH-S. **g** A general scheme of events shown
211 in this figure. For associated data see Supp. info S4.
212

213 With a co-culture MH-S macrophages and LA-4 epithelial cells we aimed to mimic the cell populations of the
214 lung alveoli, where approximately 3-5% of the alveolar surface is populated by alveolar macrophages spread
215 over nearly confluent alveolar epithelium³³. When our co-culture is exposed to TiO₂ nanotubes, macrophages
216 internalize them, but cannot entirely prevent them from reaching epithelial cells (movie in supplement S0i )
217 due to their slow rate of cleaning nanoparticles from the epithelial surface. Aside from that, macrophages also
218 slow down considerably after having taken up large amounts of nanoparticles (graph in supplement S4e),
219 making them even less efficient. Thus, the exposed epithelium unavoidably produces cauliflowers also in our
220 co-culture (supplement S0), reproducing bio-nano agglomerates observed *in vivo*¹².

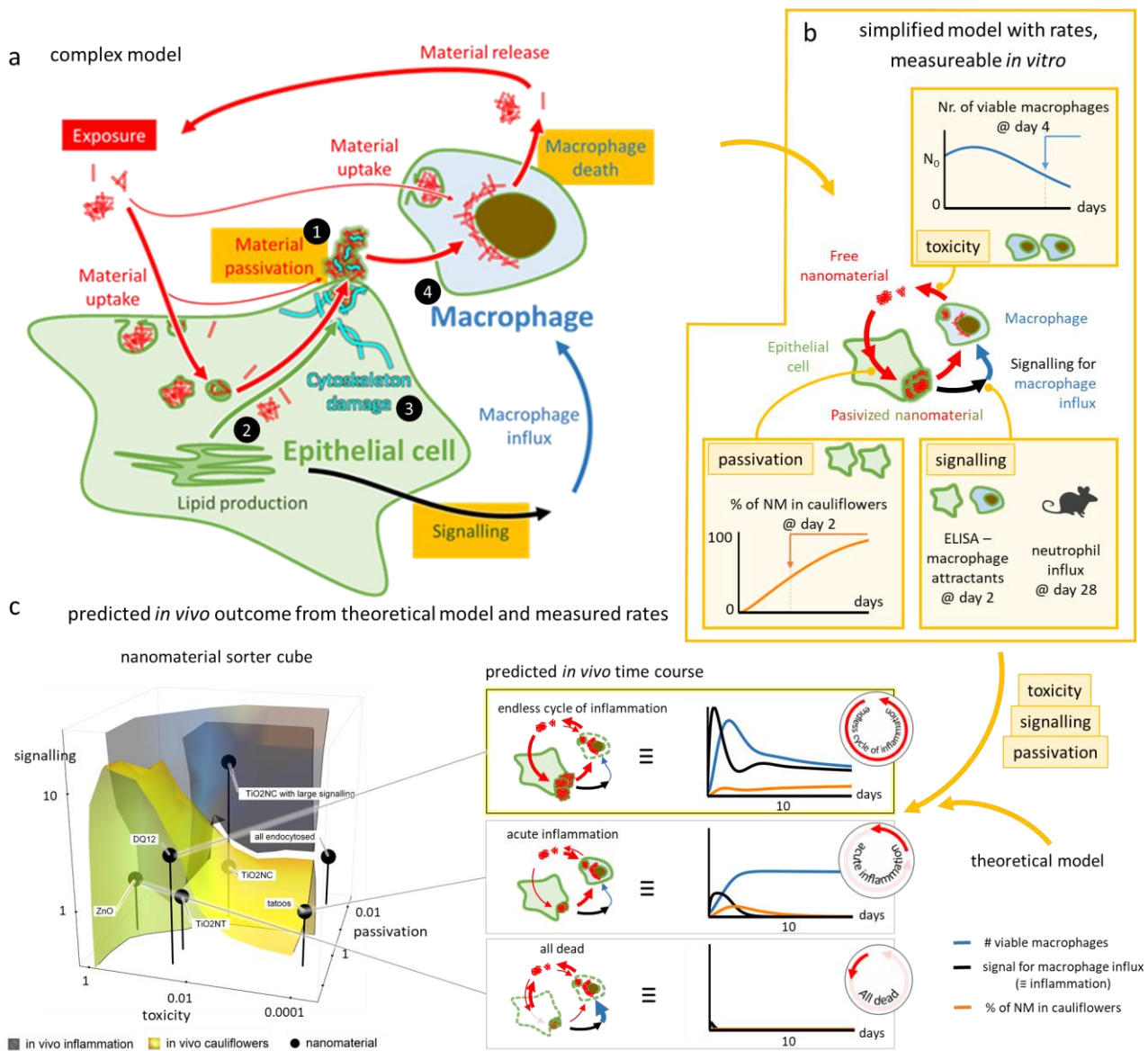
221 Although the nanoparticles are passivated in cauliflowers on the surface of LA-4 enabling their survival, the
222 same structures trigger the attack of macrophages, as seen in the experiment when unexposed macrophages
223 were added to pre-exposed epithelium with cauliflowers (Fig. 4a). After internalisation of the agglomerates,
224 macrophages are able to digest their organic part as revealed by decreased lifetime of probes on the
225 nanoparticles, indicating denser packing of nanoparticles in macrophages compared to cauliflowers (FLIM maps
226 in Fig. 4a insets). Unwrapping the passivated nanoparticles exposes the macrophage interior to their bare
227 surface, leading to the same end-state as after nanoparticle uptake by macrophages in monoculture. Such a
228 situation evidently leads to macrophage death and disintegration (Fig. 4d (4 days), 3D in supplement S4d )
229 likely due to the lack of additional lipid synthesis, as supported by genomics (Fig. 2c). A similar fate of
230 macrophages is observed also after they have attacked a whole epithelial cell (Fig. 4e, movie in supplement S4e
231 ) or a contaminated macrophage (Fig. 4f, 3D in supplement S4e ). When nanomaterial-exposed
232 macrophages die, they release bare nanomaterial, which is later (re)uptaken by epithelial cells. This can be
233 observed experimentally: after nanomaterial-laden macrophages were added to the unexposed epithelial layer,
234 nanoparticles could be seen to enter epithelial cells (Fig. 4b).

235 Such reuptake would lead to fully passivated nanomaterial on the self-protected epithelial cells. *In vivo* however,
236 dead macrophages are replaced by the influx of new monocyte-derived macrophages, attracted to the site by
237 chemokines such as C-C motif ligand 3 (CCL3, aka macrophage inflammatory protein 1-alpha, MIP-1-alpha)
238 ^{12,26}. The macrophage influx brings the entire system to conditions very similar to the initial exposure, while
239 reuptake of nanomaterial by epithelium closes the chain of events, together forming a vicious cycle of endless
240 inflammation (Fig. 4g, Fig. 5a), which has never been shown before.

241 Strikingly, the same chemokine expressions can be detected both *in vivo* and *in vitro*, but exclusively in the co-
242 culture of LA-4 and MH-S cells (Fig. 4c, purple arrows) and not in either of the monocultures of LA-4 (Fig. 4c,
243 red arrows) or MH-S (Fig. 4c, blue arrows). This would imply that the *in vitro* co-culture can reproduce the cell
244 states under *in vivo* chronic inflammation conditions. Can we predict such an *in vivo* outcome by measuring
245 states of simple *in vitro* tests?

246

247 5. Towards predictive toxicology



248

249 **Fig. 5: Cycle of uptake, passivation and release of nanomaterial between epithelial cells and macrophages**
 250 ***in co-cultures.*** **a** A grand scheme connecting all inter- and intracellular events from Figures 1 – 4, simplified
 251 to **b** a theoretical model, defined by rates of passivation, toxicity and signalling. These rates can be measured
 252 *in vitro* or *in vivo* at a single time-point. **c** By combining the measured rates and the simple model, the time
 253 course (right) is determined and nanoparticles are sorted according to their predicted outcome (left). Chronic
 254 inflammation is defined as elevated macrophage influx for longer than 10 days (area above the black contour,
 255 black line in time-courses, right). Presence of cauliflowers after 10 days is observed below the yellow contour
 256 (orange line in time-courses, right). For associated data see Supp. info S5.

257

258 The discovered complex pathway (Fig. 5a) describing a causal relationship between an acute exposure to
 259 nanoparticles and chronic inflammation conditions allows us to construct a simplified cyclical theoretical model
 260 defined with three descriptors, measurable in appropriate *in vitro* setups for each nanomaterial of interest (Fig.
 261 5b):

262 1) capacity of epithelial cells to passivate nanomaterial is measured via the fraction of nanomaterial in
 263 cauliflowers in LA-4 monoculture after 2 days (Fig. 5b, passivation);

264 2) efficiency of signaling and monocyte influx replacing the dying macrophages is measured either via
265 macrophage attractants in *in vitro* co-culture of LA-4 and MH-S after 2 days or via polymorphonuclear cell
266 influx *in vivo* after 28 days (Fig. 5b, signalling);

267 3) toxicity of the nanomaterials to individual cells is measured via the number of viable macrophages in MH-
268 S monoculture after 4 days (Fig. 5b, toxicity).

269 Whether the cycle stops or goes on indefinitely, heavily depends on the rates of the associated processes,
270 calculated from the measured descriptors as described in (supplement S5). Using these rates, the model can
271 simulate the *in vivo* time courses of nanomaterial passivated in cauliflowers, signaling for macrophage influx,
272 as well as of the total macrophage number, and accordingly predict the nanomaterial-specific acute-to-chronic
273 inflammation outcome (Fig. 5c - time traces). For example, a very toxic nanomaterial such as ZnO, exhibits a
274 rapid decline in the number of all cells, preventing passivation as well as influx of new macrophages, resulting
275 in destruction of the alveolar layer³⁴. A material similar to TiO₂ nanocubes with intermediate toxicity and
276 passivation rate, shows transient inflammation only, with all nanomaterial ending up in cells, as observed *in*
277 *vivo*¹². Finally, for a material such as TiO₂ nanotubes with intermediate toxicity and high passivation rate,
278 persistently high inflammation and large cauliflowers are predicted (Fig. 1b) in line with previous studies¹². In
279 this three-dimensional space of nanomaterial descriptors (Fig. 5c - 3D plot), we can now delineate regions
280 eliciting similar outcomes, thus sorting nanomaterials into several classes according to their mode-of-action.

281 This approach holds significant predictive value for long-term *in vivo* behavior based on outcomes of simple
282 high-throughput *in vitro* measurements. The nonlinear understanding of adverse outcome pathway initiation
283 which is crucial for understanding nanomaterial-induced chronic inflammation may also underlie cancer,
284 fibrosis, and other chronic diseases.

285

286 Methods

287 Materials

288 Alexa Fluor 647 NHS ester (Thermo Fisher), Star 520 SXP NHS ester (Abberior), ATTO 594 NHS ester (Atto-
289 tec), CellMask Orange (Invitrogen), SiR Actin (Cytoskeleton), Star Red-DPPE (Abberior), 4-(8,9-Dimethyl-
290 6,8-dinonyl-2-oxo-8,9-dihydro-2H-pyran[3,2-g]quinolin-3-yl)-1-(3-(trimethylammonio) propyl)pyridin-1-
291 ium dibromide(SHE-2N), 3-(Benzo[d]thiazol-2-yl)-6,8,9-tetramethyl-2-oxo-8,9-dihydro-2H-pyran[3,2-
292 g]quinoline-4-carbonitrile (SAG-38), LCIS-Live Cell Imaging Solution (Invitrogen), PBS-phosphate buffer
293 saline (Gibco), 100x dcb: 100-times diluted bicarbonate buffer (pH 10, osmolarity 5 miliosmolar, mixed in-
294 house), F-12K cell culture medium (Gibco), RPMI 1640 cell culture medium (Gibco), Trypsin (Sigma),
295 Penicillin-Streptomycin (Sigma), Non-essential amino acids (Gibco), Beta mercaptoethanol (Gibco), glucose
296 (Kemika), BSA-bovine serum albumin (Sigma), Hydrogen peroxide (Merck), Chlorpromazine (Alfa Aesar),
297 MBCD-Metyl-Beta-Cyclodextran (Acros organics), Resveratrol (Sigma), #1.5H □-dishes (Ibidi,) #1.5H □-
298 Slide 8-well (Ibidi), Limulus Amebocyte Lysate Assay (Lonza, Walkersville, MD, USA), 10% neutral buffered
299 formalin (CellPath Ltd, UK), haematoxylin and eosin (H&E), Pelcotec™ SFG12 Finder Grid Substrate- Si
300 wafers (Ted Pella), Aeroneb®Pro nebulizer (from VITROCELL® Cloud 6 system), GeneChip® WT PLUS
301 Reagent Kit (Thermo Fisher/Affymetrix)

302 Nanomaterials used in this study

303 Synthesized in-house by P. Umek:

304 name: TiO₂ nanotubes and TiO₂ nanocubes;

305 Official ID: PU-nTOX-01-03, PU-nTOX-01-21

306

307 Kind gift from U. Vogel:

308 name: Carbon black, MKNA015, MKNA100 and SiO₂ DQ12;

309 JRC ID: Printex 90, MKN- TiO₂ -A015, MKN- TiO₂ -A100, NA .

310

311 Kind gift from JRC:

312 JRC ID: NM101 TiO₂ anatase, NM105 TiO₂ rutil-anatase, NM200 Silica, NM402 MWCNT, NM401 MWCNT,
313 NM110 ZnO and NM 111 ZnO;
314 JRC ID: JRCNM01001a, JRCNM01005a, JRCNM02000a, JRCNM04002a, JRCNM04001a, JRCNM01101a,
315 JRCNM62101a

316

317 Cell culture

318

319 Murine epithelial lung tissue cell line (LA- 4; cat. no. ATCC CCL-196) and murine alveolar lung macrophage
320 (MH-S; cat. No. CRL2019) cell line were purchased from and cultured according to American Type Culture
321 Collection (ATCC) instructions. Cells were cultured in TPP cell culture flasks at 37 °C in a 5% CO₂ humidified
322 atmosphere until monolayers reached desired confluency. All experiments were performed with cells before the
323 twentieth passage. For long-term live cell experiments we used a homemade stage top incubator which
324 maintains a humidified atmosphere with a 5% CO₂ heated on 37 °C.

325 Medium used for culturing of the epithelial LA-4 cells is Ham's F-12K medium (Gibco) supplemented with
326 15% FCS (ATCC), 1% P/S (Sigma), 1% NEAA (Gibco), 2 mM L-gln.

327 For alveolar macrophages, MH-S, cell line we used RPMI 1640 (Gibco) medium supplemented with 10% FCS
328 (ATCC), 1% P/S (Sigma), 2 mM L-gln, and 0.05 mM beta mercapthoethanol (Gibco).

329

330 Nanomaterial synthesis and labelling

331

332 The TiO₂ anatase nanotubes used in this paper were synthesized, functionalized with AEAPMS, and labelled
333 with STED-compatible fluorescent probes via a covalent reaction between the AEAPMS and ester functional
334 group on the probe. All this was done in-house as described in ²⁷. Labelled TiO₂ was then stored in 100x diluted
335 bicarbonate buffer. For the multi-NM exposure experiments we used other NMs as well. All the NMs were
336 suspended in PBS and sonicated in ice bath using a tip sonicator (Sonicator 4000, Misonix, with 419 Microtip
337 probe) for 15 min with 5s ON/ 5s OFF steps.

338 The average hydrodynamic particle size of the TiO₂ tube in suspension (3.24 mg/ ml) was determined by
339 Dynamic Light Scattering (DLS). The TiO₂ tube suspension had a bimodal size distribution with a major peak
340 at 60 nm and a narrow peak at 21 nm (Danielsen 2019 TAAP). The intensity-based z-average size was 168.7
341 nm and the polydispersity index (PI) was 0.586, indicating some polydispersity in the suspensions. Endotoxin
342 levels were measured using the Limulus Amebocyte Lysate Assay. The level of endotoxins was low in TiO₂
343 nanotube suspensions (0.095 endotoxin units (EU)/mL), and in nanopure water with 2 % mouse serum (0.112
344 EU/ml, self-extracted).

345

346 *In vitro* sample preparation and exposure of MH-S&LA-4 to TiO₂

347

348 LA-4 and MH-S cells were seeded in Ibidi 1.5H dishes of various surface area, depending on the experiment.
349 After 24 h NM (c=1mg/mL) was added in a 1:1, 10:1 and 100:1 (NM_{surface} : Cell_{surface}) ratios, according to the
350 experiment needs. Before exposure, NM suspension was sonicated for 10s in an ultrasonic bath (Bransonic
351 ultrasonic cleaner, Branson 2510EMT). Cells were then incubated at 37°C and 5% CO₂ atmosphere with the
352 NM for the following 24 h, 48 h or longer in order to observe the cells at the post-exposure time points of
353 interest. If the experiment required monoculture of either cell line, sample were prepared as described above, if
354 however, we experimented with the co-cultures, sample preparation differed slightly. For co-cultures, we grew
355 LA-4 and MH-S in separate dishes up to desired confluency (lower than for monocultures) and then mixed them
356 together by adding MH-S in the LA-4 dish (1 : 40). Co-cultures were then incubated for 24 h more, exposed to
357 NM as described above and incubated for additional desired amount of time. Growth medium for co-cultures
358 was mixture of equal volumes of F12K and RPMI 1640. Cells were then labelled with fluorescent dyes

359 according to the manufacturers recommendations. Unbound fluorescent label was washed and medium was
360 exchanged for LCIS.

361
362 In some experiments we used different chemicals for modulation of the metabolism. For blocking the CME,
363 cells were treated with 100 μ M Chlorpromazine for 15 min. Membrane cholesterol was extracted with 24 h
364 incubation with 0.5 - 1 mM MBCD. FAS was inhibited with overnight 100 μ M Resveratrol incubation. Finally,
365 for actin stabilization, we used higher concentration (≥ 1 mM) of Sir-Actin Label based on Jasplankinolide. All
366 the chemical modulators were added before exposure to NM and incubated with the NM for abovementioned
367 time periods.

368
369 For the reuptake experiments different cell lines were grown separately and aspirate of one cell culture was
370 added in the other and then observed.

371
372 HIM, SEM

373 Samples were prepared as usual but we grew them on Si-wafers. After reaching desired confluency samples
374 were freeze-dried with metal mirror freezing technique.

375
376 Transcriptomics

377 Samples were prepared as described. Cells were exposed to TiO₂ and MWCNT for 4 h and 48 h. From exposed
378 and control samples (control at 0 h and 48 h) growth medium was removed from the wells and frozen at -70°C
379 with the 6-well plates containing cells only. RNA samples for the whole transcriptome expression were prepared
380 with the GeneChip® WT PLUS Reagent Kit (Thermo Fisher/Affymetrix) and analysed with the
381 GeneChip™ Whole Transcript (WT) Expression Arrays according to the manufacturers guidelines.

382 Statistical analysis for all probe sets includes limma t-test and Benjamini-Hochberg multiple testing correction.
383 Significant genes were determined with a False Discovery Rate (FDR) < 10%. Also, the p-values of the limma t-
384 test was used to define sets of regulated genes (p < 0.01/0.05). p-values were used to exclude background signals:
385 significant genes were filtered for p < 0.05 in more than half of the samples in at least one group (indicated by
386 “dabg”, data above background).

387 In the arrow graphs, only genes which were up- or down-regulated more than two times compared to non-
388 exposed cells are shown. The signal (x axis) is drawn in logarithmic scale. Expression is normalized to
389 expression of control samples.

390
391 Detailed protocols are available in supplement material.

392
393 *Imaging in vitro*

394 STED

395 Super-resolution and confocal fluorescence micrographs were acquired using custom build STED microscope
396 from Abberior with an Olympus IX83 microscope and two avalanche photodiodes as detectors (APDs). Images
397 have been acquired using Imspector (version 16.2.8282-metadata-win64-BASE) software also provided by
398 Abberior. Microscope is equipped with two 120 picosecond pulsed laser sources (Abberior) with excitation
399 wavelengths 561 and 640 nm and maximal power of 50 μ W in the sample plane. Pulse repetition frequency for
400 experiments was 40 - 80 MHz, depending on the experiment. STED depletion laser wavelength is 775 nm with
401 same repetition frequency as excitation lasers, pulse length of 1.2 ns and maximal power of 170 mW in the
402 sample plane. Filter sets used for detection have been 605–625 nm (green channel), 650–720 nm (red channel).
403 All the microscope settings that have been tuned separately for maximal resolution during each of the
404 experiments have been recorded and given with the experiment images in Supplement. The combinations of
405 excitation and filter sets have also been optimized for each experiment if necessary.

406 FLIM

407 Fluorescence lifetime images (FLIM) were obtained on the same custom-built STED microscope (Abberior
408 instruments) as confocal and STED fluorescence images in this study. The sample was excited by pulsed laser
409 sources with wavelengths 561 nm and 640 nm and the emitted fluorescence was detected using PMT detectors

410 and TCSPC technology developed by Becker & Hickl. 16-channel GaASP PMT detectors attached to a
411 spectrograph with diffraction grating 600 l/mm were used to measure fluorescence lifetime of emitted photons
412 with wavelengths ranging from 560 to 760 nm. Spectral information was discarded and the lifetimes were
413 gathered in Inspector 16.2 (Abberior Instruments).

414

415 The fluorescence lifetime data was analysed with SPCImage 7.3 (Becker & Hickl) software, where the Decay
416 matrix was calculated from the brightest pixel in the image (monoexponential fitting), binning was set to 3 and
417 threshold to 5. The rainbow LUT was rescaled to range from 500 ps to 1000 ps and intensity and contrast of the
418 lifetime-coded image were adjusted for easier comparison between experiments.

419

420 **Imaging of nanomaterial in backscatter mode:**

421 Simultaneously with measuring fluorescence from CellMask Orange in the cell membrane (as described in
422 STED section), backscattered light was detected as well to locate the nanomaterial in the sample. A tunable
423 Chameleon Discovery laser (Coherent) with 100 fs long pulses, pulse repetition frequency 80 MHz, and
424 maximal average power of 1.7 W at 850 nm was used as the scattering light. The pre-attenuated laser light with
425 a wavelength of 750 nm first passed through a 785 nm built-in dichroic where a fraction of the power was
426 directed onto the sample through the same 60x WI objective (NA 1.2) as the excitation light. The backscattered
427 light then went back through the same objective and dichroic, now mostly passing through the dichroic towards
428 the detectors. After passing through a pinhole (0.63 A.U.), the backscattered light was spectrally separated from
429 the fluorescence by short-pass 725 nm dichroic, afterwards being detected on the same PMT, as described in
430 the FLIM section, this time set to collect light with wavelengths above 725nm.

431 Due to the large coherence of the laser, the backscattered light exhibited a strong speckle pattern, which was
432 diminished by a 100-nm-wide Gaussian blur on the scattering image, thus decreasing false negative
433 colocalisation of NM on account of spatial resolution.

434

435 **SEM**

436 SEM imaging has been performed on MIRA3 Flexible FE-SEM produced by TESCAN, by detection of
437 secondary electrons. Beam powers used have been between 5.0 kV and 15 kV with variable field of view 1.8
438 μm to 180 μm . All samples have been measured under high pressure vacuum (HiVac). All analysis has been
439 performed in Tescan developed software.

440

441 **HIM**

442 Super-resolution imaging on the nanoscale was carried out using Helium Ion Microscope (Orion NanoFab,
443 Zeiss) available at IBC at the Helmholtz-Zentrum Dresden - Rossendorf e. V., a member of the Helmholtz
444 Association. Microscope equipped with GFIS injection system and additional in-situ backscatter spectrometry
445 and secondary ion mass spectrometry can achieve 0.5 nm lateral resolution imaging using 10-35 keV He ion
446 beams. Measurements of secondary electrons (Se) emitted from the first few nm of the sample were done by He
447 ion acceleration of 30 keV, current of 1.7 pA and were acquired under high vacuum inside the sample chamber
448 (3×10^{-7} mBar). Field-of-view was varied from 60 μm x 60 μm down to 1 μm x 1 μm , with pixel steps small as
449 2nm. Imaging was performed on non-tilted and tilted sample stage (45 degrees) for better 3-D visualization.

450 *In vivo* data – U. Vogel group

451

452 The materials and methods used for intratracheal instillation of mice with TiO₂ tube are described in detail by
453 Danielsen et. al ¹² and included here in an abbreviated version.

454 Preparation and characterization of TiO₂ tube suspensions TiO₂ tubes were characterization in
455 Urbančič et. al ²⁷.

456

457 TiO₂ tubes were suspended in nanopure water with 2 % v/v mouse serum (prepared in-house) to a final
458 concentration of 3.24 mg/ml. The suspension was probe sonicated on ice for 16 min with 10 % amplitude. 3.24
459 mg/ml corresponds to a dose of 162 µg TiO₂ tube per 50 µl instillation volume per mice. The vehicle of nanopure
460 water with 2 % v/v mouse serum was probe sonicated using the same protocol. The dose of 162 µg/mouse (3:1
461 NM_{surface} : Cell_{surface} in vitro) is equivalent to 15 working days at the 8-h time-weighted average occupational
462 exposure limit for TiO₂ by Danish Regulations (6.0 mg/m³ TiO₂).

463

464 Animal handling and exposure

465 Seven-week-old female C57BL/6jBomTac mice (Taconic, Ejby, Denmark) were randomized in groups for TiO₂
466 tube exposure (N=5 mice/group for histology) and vehicle controls (N = 2-4 mice/group). At 8 weeks of age the
467 mice were anaesthetized and exposed to 0 µg or 162 µg TiO₂ tube in 50 µl vehicle by single intratracheal
468 instillation. In brief, the mice were intubated in the trachea using a catheter. The 50 µl suspension was instilled
469 followed by 200 µL air. The mouse was transferred to a vertical hanging position with the head up. This ensures
470 that the administered material is maintained in the lung. Animal experiments were performed according to EC
471 Directive 2010/63/UE in compliance with the handling guidelines established by the Danish government and
472 permits from the Experimental Animal Inspectorate (no. 2015-15-0201-00465). Prior to the study, the
473 experimental protocols were approved by the local Animal Ethics Council.
474 More details regarding the animal study can be found in Danielsen et al.¹².

475

476 Histology and enhanced darkfield imaging

477 At 28, 90 or 180 days post-exposure mice were weighed and anesthetized. Lungs were filled slowly with 4%
478 formalin under 30 cm water column pressure. A knot was made on the trachea to secure formaldehyde in lungs
479 to fixate tissue in “inflated state”. Lungs were then removed and placed in 4% neutral buffered formaldehyde
480 for 24 hours. After fixation the samples were trimmed, dehydrated and embedded in paraffin. 3 µm thin sections
481 were cut and stained with haematoxylin and eosin (H&E). Cytoviva enhanced darkfield hyperspectral system
482 (Auburn, AL, USA) was used to image particles and organic debris in the histological sections of mouse lungs.
483 Enhanced darkfield images were acquired at 100x on an Olympus BX 43 microscope with a Qimaging
484 Retiga4000R camera.

485

486 Modelling

487 *In silico* data – atomistic molecular dynamics simulation

488 System composition

489 Atomistic molecular dynamics simulations have been carried out for DMPC and POPE lipids near anatase (101)
490 TiO₂ surface in water environment. Anatase slab (71.8 x 68.2 x 30.5 Å) with (101) surface normal to the z axis
491 is used as a model of a nanoparticle surface. The slab contains 4536 Ti atoms of which 504 are five-fold
492 coordinated atoms on the surface. (101) anatase surface was chosen as a surface of the lowest energy. At neutral
493 pH TiO₂ surface is covered by hydroxyl groups and is negatively charged. In our model we bind hydroxyl groups
494 to 5-coordinated surface Ti atoms so that the surface charge density is close to the experimental value at neutral
495 pH. Thus we add 151 hydroxyl groups to randomly picked Ti surface atoms (which constitutes 30% of their
496 total amount) which results in a surface charge density of -0.62 electrons/nm², which is in line with the
497 experimental results³⁵.

498

499 The TiO₂ slab is then placed in the middle of the simulation box with 3D periodic boundary conditions. The box
500 size in X and Y directions is defined by the slab length and width so that the slab is periodic in those directions.
501 The height of the box is set to 130 Å to accommodate the TiO₂ slab (thickness of 30.5 Å), eventual formed lipid
502 bilayer on the both sides (2 x 40 Å) as well as their hydration layers (2 x 10 Å). 82 lipid molecules (POPE or
503 DMPC) are inserted at random unoccupied positions in the box in random orientations, after that the box is
504 filled with water molecules (about 12000). Then, a small number of water molecules are picked at random and

505 are substituted with Na⁺ and Cl⁻ ions to balance the negative surface charge of the slab and provide NaCl
506 concentration of 0.15 M in the water phase of the simulated system.

507 Simulation protocol

508 First, energy minimization of the simulated systems using the steepest gradient descent method is performed,
509 followed by a short 100 ps pre-equilibration run at constant volume and temperature. After that, the pressure in
510 the system is equilibrated to 1 bar using anisotropic Berendsen barostat³⁶ with relaxation time of 5 ps during 10
511 ns, which is finally followed by 1 μ s production run in the NVT ensemble. Leap-frog algorithm with time step
512 1 fs is used to integrate the equations of motion. Center-of-mass motion is removed every 100 steps. Verlet cut-
513 off scheme³⁷ with the buffer tolerance of 0.005 kJ x mol⁻¹ x ps⁻¹ per atom is used to generate the pair lists.
514 Minimum cut-off of 1.4 nm is used for both short ranged electrostatic and VdW interactions. Long range
515 electrostatics are calculated using PME³⁸ with the grid spacing of 0.12 nm and cubic interpolation. Long range
516 dispersion corrections are applied to both energy and pressure. Velocity rescaling thermostat³⁹ is used to control
517 the temperature, which is set to 303 K with the relaxation time of 1 ps. All bonds with hydrogen atoms are
518 constrained using the LINCS algorithm⁴⁰. Atom coordinates and energies are saved every 5 ps. All simulations
519 were performed by the Gromacs 2019 software package⁴¹. Visualization of the simulations is done by VMD⁴².

520 Models used

521 Lipids are described by the Slipids force field⁴³. For TiO₂, we use parameters optimized to fit results on charge
522 density distributions and water-TiO₂ surface coordination obtained in *ab-initio* simulations of TiO₂-water
523 interface⁴⁴. These parameters are listed in tables in supplement S5b, S5c and S5d. Water molecules are
524 represented by the TIP3P model⁴⁵, and for Na⁺ and Cl⁻ ions Yoo and Aksimentiev ion parameters is used⁴⁶.
525 Lorentz-Berthelot rules are applied to determine Lennard-Jones parameters for cross-interactions.

526 Model of chronic inflammation following NM exposure

527 The theoretical model of chronic inflammation following NM exposure is described by a series of differential
528 equations, describing the events observed in *in vitro* and *in vivo* experiments in this work. This minimal-
529 complexity *in vivo* model consists of 6 variables (surface of NM in epithelial cells, in cauliflowers, in
530 macrophages and freely-floating NM, surface of macrophages and surface of epithelial cells), 4 locked
531 parameters (endocytosis rate, rate of cauliflower endocytosis, delay, and epithelial cell replication rate) and 3
532 NM-associated parameters (cauliflower formation rate, signalling efficiency, and toxicity), which change from
533 nanomaterial to nanomaterial. Separate *in vitro* models were obtained from the *in vivo* model by swapping the
534 macrophage influx with macrophage replication and leaving out non-existent cells for monocultures.

535 The system of equations was solved numerically using Wolfram Mathematica 12.0, licence L5063-5112 to
536 obtain the time evolution and final state of the model. The same software was also used for visualization of the
537 results.

538 The phase space was scanned by calculating the time evolution of the appropriate system of equations from
539 chapter S5b for a set of nanomaterials with appropriately interspaced parameters: toxicity (*tox*), cauliflower
540 formation (*cff*) and signalling efficiency (*signalEff*). For each parameter, 30 logarithmically-equally-spaced
541 values in a sensible range were chosen – the total amount of values in the grid was thus 30 x 30 x 30 = 27.000.

542 More information can be found in S5b, S5c and S5d.

543 Software

544 Inspector (version 16.2.8282-metadata-win64-BASE) software provided by Abberior

545 SPCImage 7.3 (Becker & Hickl)

546 Fiji, ImageJ 1.52p (NIH)

547 syGlass (<http://www.syglass.io/>, RRID:SCR_017961)

548 Mathematica 12.0, licence L5063-5112 (Wolfram)

549 genomics software: GSEA by Broad Institute
550 modelling: GROMACS (calculation), VMD (visualisation)
551

552 Data availability

553 Source data is available online at <http://lbfnanobiodatabase.ijs.si/file/data/cauliflowerpaper/> with all 3Ds and
554 movies as a part of a database develop for H2020 Smart Nano Tox project.

555 References

- 556 1. Netea, M. G. *et al.* A guiding map for inflammation. *Nat. Immunol.* **18**, 826–831 (2017).
- 557 2. Furman, D. *et al.* Chronic inflammation in the etiology of disease across the life span. *Nat. Med.* **25**,
558 1822–1832 (2019).
- 559 3. Roth, G. A. *et al.* Global, regional, and national age-sex-specific mortality for 282 causes of death in 195
560 countries and territories, 1980–2017: a systematic analysis for the Global Burden of Disease Study 2017.
561 *The Lancet* **392**, 1736–1788 (2018).
- 562 4. Underwood, E. The polluted brain. *Science* **355**, 342–345 (2017).
- 563 5. OECD. OECD Environmental Outlook to 2050. doi:<http://dx.doi.org/10.1787/9789264122246-en>.
- 564 6. WHO. Air pollution. <https://www.who.int/westernpacific/health-topics/air-pollution>.
- 565 7. EPA/600/R-12/056F Provisional Assessment of Recent Studies on Health Effects of Particulate Matter
566 Exposure. (2012).
- 567 8. Rohr, J. R., Salice, C. J. & Nisbet, R. M. Chemical safety must extend to ecosystems. *Science* **356**, 917–
568 917 (2017).
- 569 9. Huh, D. *et al.* Reconstituting Organ-Level Lung Functions on a Chip. *Science* **328**, 1662–1668 (2010).
- 570 10. Maynard, A. D. & Aitken, R. J. ‘Safe handling of nanotechnology’ ten years on. *Nat. Nanotechnol.* **11**,
571 998–1000 (2016).
- 572 11. Nel, A. E. & Malloy, T. F. Policy reforms to update chemical safety testing. *Science* **355**, 1016–1018
573 (2017).
- 574 12. Danielsen, P. H. *et al.* Effects of physicochemical properties of TiO₂ nanomaterials for pulmonary
575 inflammation, acute phase response and alveolar proteinosis in intratracheally exposed mice. *Toxicol.*
576 *Appl. Pharmacol.* **386**, 114830 (2020).

- 577 13. Fujita, K. *et al.* Intratracheal instillation of single-wall carbon nanotubes in the rat lung induces time-
578 dependent changes in gene expression. *Nanotoxicology* **9**, 290–301 (2015).
- 579 14. Cho, W.-S. *et al.* NiO and Co₃O₄ nanoparticles induce lung DTH-like responses and alveolar
580 lipoproteinosis. *Eur. Respir. J.* **39**, 546–557 (2012).
- 581 15. van den Brule, S. *et al.* Nanometer-long Ge-imogolite nanotubes cause sustained lung inflammation and
582 fibrosis in rats. *Part. Fibre Toxicol.* **11**, 67 (2014).
- 583 16. Tian, F. *et al.* Pulmonary DWCNT exposure causes sustained local and low-level systemic inflammatory
584 changes in mice. *Eur. J. Pharm. Biopharm.* **84**, 412–420 (2013).
- 585 17. Kim, S.-H. *et al.* The early onset and persistent worsening pulmonary alveolar proteinosis in rats by
586 indium oxide nanoparticles. *Nanotoxicology* **0**, 1–11 (2019).
- 587 18. Kasai, T. *et al.* Lung carcinogenicity of inhaled multi-walled carbon nanotube in rats. *Part. Fibre Toxicol.*
588 **13**, 53 (2016).
- 589 19. Kasai, T. *et al.* Thirteen-week study of toxicity of fiber-like multi-walled carbon nanotubes with whole-
590 body inhalation exposure in rats. *Nanotoxicology* **9**, 413–422 (2015).
- 591 20. Pauluhn, J. Subchronic 13-week inhalation exposure of rats to multiwalled carbon nanotubes: toxic effects
592 are determined by density of agglomerate structures, not fibrillar structures. *Toxicol. Sci. Off. J. Soc.*
593 *Toxicol.* **113**, 226–242 (2010).
- 594 21. Hotamisligil, G. S. Inflammation and metabolic disorders. *Nature* **444**, 860–867 (2006).
- 595 22. Röhrig, F. & Schulze, A. The multifaceted roles of fatty acid synthesis in cancer. *Nat. Rev. Cancer* **16**,
596 732–749 (2016).
- 597 23. Peck, B. & Schulze, A. Lipid Metabolism at the Nexus of Diet and Tumor Microenvironment. *Trends*
598 *Cancer* **5**, 693–703 (2019).
- 599 24. Qiao, Y. *et al.* FABP4 contributes to renal interstitial fibrosis via mediating inflammation and lipid
600 metabolism. *Cell Death Dis.* **10**, 382 (2019).
- 601 25. Bourdon, J. A. *et al.* Hepatic and pulmonary toxicogenomic profiles in mice intratracheally instilled with
602 carbon black nanoparticles reveal pulmonary inflammation, acute phase response, and alterations in lipid
603 homeostasis. *Toxicol. Sci. Off. J. Soc. Toxicol.* **127**, 474–484 (2012).

- 604 26. Poulsen, S. S. *et al.* Changes in cholesterol homeostasis and acute phase response link pulmonary
605 exposure to multi-walled carbon nanotubes to risk of cardiovascular disease. *Toxicol. Appl. Pharmacol.*
606 **283**, 210–222 (2015).
- 607 27. Urbančič, I. *et al.* Nanoparticles Can Wrap Epithelial Cell Membranes and Relocate Them Across the
608 Epithelial Cell Layer. *Nano Lett.* **18**, 5294–5305 (2018).
- 609 28. Pollard, T. D. & Cooper, J. A. Actin, a Central Player in Cell Shape and Movement. *Science* **326**, 1208–
610 1212 (2009).
- 611 29. Tran, D. T., Masedunskas, A., Weigert, R. & Hagen, K. G. T. Arp2/3-mediated F-actin formation controls
612 regulated exocytosis in vivo. *Nat. Commun.* **6**, 1–10 (2015).
- 613 30. Khaitlina, S. Y. Intracellular transport based on actin polymerization. *Biochem. Biokhimiia* **79**, 917–927
614 (2014).
- 615 31. Li, P., Bademosi, A. T., Luo, J. & Meunier, F. A. Actin Remodeling in Regulated Exocytosis: Toward a
616 Mesoscopic View. *Trends Cell Biol.* **28**, 685–697 (2018).
- 617 32. Tran, D. T. & Ten Hagen, K. G. Real-time insights into regulated exocytosis. *J. Cell Sci.* **130**, 1355–1363
618 (2017).
- 619 33. Laskin, D. L., Malaviya, R. & Laskin, J. D. Chapter 32 - Pulmonary Macrophages. in *Comparative*
620 *Biology of the Normal Lung (Second Edition)* (ed. Parent, R. A.) 629–649 (Academic Press, 2015).
621 doi:10.1016/B978-0-12-404577-4.00032-1.
- 622 34. Gosens, I. *et al.* Comparative Hazard Identification by a Single Dose Lung Exposure of Zinc Oxide and
623 Silver Nanomaterials in Mice. *PLoS ONE* **10**, (2015).
- 624 35. Akratopulu, K. C., Vordonis, L. & Lycourghiotis, A. Effect of temperature on the point of zero charge
625 and surface dissociation constants of aqueous suspensions of γ -Al₂O₃. *J. Chem. Soc. Faraday Trans. 1*
626 *Phys. Chem. Condens. Phases* **82**, 3697–3708 (1986).
- 627 36. Berendsen, H. J. C., Postma, J. P. M., van Gunsteren, W. F., DiNola, A. & Haak, J. R. Molecular
628 dynamics with coupling to an external bath. *J. Chem. Phys.* **81**, 3684–3690 (1984).
- 629 37. Páll, S. & Hess, B. A flexible algorithm for calculating pair interactions on SIMD architectures. *Comput.*
630 *Phys. Commun.* **184**, 2641–2650 (2013).

- 631 38. Darden, T., York, D. & Pedersen, L. Particle mesh Ewald: An $N \cdot \log(N)$ method for Ewald sums in large
632 systems. *J. Chem. Phys.* **98**, 10089–10092 (1993).
- 633 39. Bussi, G., Donadio, D. & Parrinello, M. Canonical sampling through velocity rescaling. *J. Chem. Phys.*
634 **126**, 014101 (2007).
- 635 40. Hess, B. P-LINCS: A Parallel Linear Constraint Solver for Molecular Simulation. *J. Chem. Theory*
636 *Comput.* **4**, 116–122 (2008).
- 637 41. Abraham, M. J. *et al.* GROMACS: High performance molecular simulations through multi-level
638 parallelism from laptops to supercomputers. *SoftwareX* **1–2**, 19–25 (2015).
- 639 42. Humphrey, W., Dalke, A. & Schulten, K. VMD: visual molecular dynamics. *J. Mol. Graph.* **14**, 33–38,
640 27–28 (1996).
- 641 43. Jämbeck, J. P. M. & Lyubartsev, A. P. Derivation and Systematic Validation of a Refined All-Atom Force
642 Field for Phosphatidylcholine Lipids. *J. Phys. Chem. B* **116**, 3164–3179 (2012).
- 643 44. Agosta, L., Brandt, E. G. & Lyubartsev, A. P. Diffusion and reaction pathways of water near fully
644 hydrated TiO₂ surfaces from ab initio molecular dynamics. *J. Chem. Phys.* **147**, 024704 (2017).
- 645 45. Jorgensen, W. L., Chandrasekhar, J., Madura, J. D., Impey, R. W. & Klein, M. L. Comparison of simple
646 potential functions for simulating liquid water. *J. Chem. Phys.* **79**, 926–935 (1983).
- 647 46. Yoo, J. & Aksimentiev, A. Improved Parametrization of Li⁺, Na⁺, K⁺, and Mg²⁺ Ions for All-Atom
648 Molecular Dynamics Simulations of Nucleic Acid Systems. *J. Phys. Chem. Lett.* **3**, 45–50 (2012).

649 Acknowledgements

650 This research was funded by EU Horizon2020 Grant No. 686098 (SmartNanoTox project), Slovenian
651 Research Agency (program P1-0060), Young Researcher Program (Hana Majaron) and Young Researcher
652 Program (Aleksandar Sebastijanović). We are also grateful to team at TeScan for ESEM measurements and
653 would like to thank dr. Gregor Hlawacek and dr. Nico Klingner for assistance on HIM. We kindly thank JRC
654 for providing us with various nanomaterials and the team from Syglass for their support.

655 Author contributions

656 These authors have contributed equally: Hana Majaron, Boštjan Kokot, Aleksandar Sebastijanović.

657

658 Affiliations

659 Department of Condensed Matter Physics, Jožef Stefan Institute, Ljubljana, Slovenia

660 Hana Majaron, Boštjan Kokot, Aleksandar Sebastijanović, Rok Podlipec, Patrycja Zawilska, Ana Krišelj, Mojca
661 Pušnik, Petra Čotar, Polona Umek, Stane Pajk, Iztok Urbančič, Tilen Koklič, Janez Štrancar

662

663 Jožef Stefan International Postgraduate School, Jamova cesta 39, 1000 Ljubljana, Slovenia

664 Hana Majaron, Aleksandar Sebastijanović

665

666 Faculty of Natural sciences and Mathematics, University of Maribor, Maribor, Slovenia

667 Boštjan Kokot

668

669 Institute of Lung Biology and Disease, Helmholtz Zentrum München, 85764 Neuherberg, Germany

670 Carola Voss, Carolina Ballester, Qiaoxia Zhou, Otmar Schmid, Martin Irmeler, Johannes Beckers, Tobias
671 Stoeger

672

673 National Research Centre for the Working Environment, Copenhagen Ø, Denmark

674 Trine Berthing, Pernille H. Danielsen, Ulla B. Vogel

675

676 Faculty of Pharmacy, University of Ljubljana, Ljubljana, Slovenia

677 Stane Pajk, Mojca Pušnik

678

679 Faculty of Mathematics and Physics, University of Ljubljana, Ljubljana, Slovenia

680 Petra Čotar

681

682 Department of Chemistry, Imperial College London, London, United Kingdom

683 Claudia Contini, Matthew Schneemilch, Nicholas Quirke

684

685 Institut Jean Lamour, CNRS-Université de Lorraine, Nancy, France

686 Olivier Joubert

687

688 School of Physics, University College Dublin, Belfield, Dublin 4, Ireland

689 Vladimir Lobaskin, Vadim Zhernovkov

690

691 Health Canada

692 Sabina Halappanavar

693

694 Department of Materials and Environmental Chemistry, Stockholm University, SE-10691 Stockholm, Sweden

695 Alexander Lyubartsev, Mikhail Ivanov

696

697 Joint Research Centre

698 Jessica Ponti

699 **Corresponding authors**

700 Correspondence to Janez Štrancar, Tilen Koklič and Tobias Stoeger.

701 **Materials & Correspondence**

702 Materials and correspondence should be addressed to H.M, B.K. or A.S.

703 **Ethics declarations**

704 **Competing interests**

705 The authors declare no competing interests.

706 **Supplementary information**

707 Supplementary information

708 This file contains the Supplementary Discussion, Supplementary References and a full guide for
709 Supplementary.

710 **Source data**

711 Is currently available upon request.